https://dx.doi.org/10.21577/0103-5053.20210130

J. Braz. Chem. Soc., Vol. 33, No. 2, 135-142, 2022

Article

Influence of the Local Structure on the Photocatalytic Properties of Zinc Spinel Ferrite Nanoparticles

Luciana B. Biazati,[a] Lucas Lorenzini,[a] Sandra A. D. Ferreira,[a] Arilza O. Porto,[,b] Eustáquio V. R. de Castro,[a] José D. Fabris,[b] Marcos B. J. G. de Freitas[a] and Maria de Fátima F. Lelis*[,a]*

[a]*Departamento de Química, CCE, Universidade Federal do Espírito Santo, Campus Goiabeiras, 29075-910 Vitória-ES, Brazil*

[b]*Departamento de Química, ICEx, Universidade Federal de Minas Gerais, Campus Pampulha, 31270-901 Belo Horizonte-MG, Brazil*

The correlation between iron distribution in octahedral or tetrahedral sites in synthetic magnetite and zinc spinel ferrites and their catalytic properties were investigated in this work. The zinc-doped nanomagnetites were prepared by co-precipitation method and annealed at 420 °C. X-ray diffraction, UV-Vis, X-ray absorption and ^{57}Fe Mössbauer spectroscopies were used to identify iron sites. The obtained results showed that Zn^{II} replaces the relatively smaller Fe^{III} cation in the tetrahedral sites, increasing the cubic lattice dimension, and this replacement remarkably enhances the catalytic effectiveness of the Zn-spinel ferrite towards the indigo carmine degradation compared to undoped magnetite. The indigo carmine degradation experiments were carried out using photo-Fenton method in which 50 mL of indigo carmine dye aqueous solutions (20 mg L^{-1}, pH 3.0), 20 mg $Zn_xFe_{(3-x)}O_4$, and 2.0 mL H_2O_2 (aqueous solution at 0.028 mol L^{-1}) were placed under UV light at 25 °C. Under these experimental conditions the degradation rate of indigo carmine was superior to 98%.

Keywords: ferrites, XANES, EXAFS, Mössbauer spectroscopy, Fenton process, indigo carmine

Introduction

Ferrite spinels are magnetic compounds containing iron, for which the general chemical stoichiometry corresponds to $\left(M_2^kO_k^{-II}\right)_{\frac{m}{2}}\left(Fe_2^{III}O_3^{-II}\right)_n$, where M is a metal cation of valence k occupying tetrahedral sites; m and n are integer numbers.[1] For magnetite, M = Fe; k = 2; m = 1 and n = 1, and the ideal formula is $[Fe^{III}]\{Fe^{III}|Fe^{II}\}O_4$, where Fe^{III} and Fe^{II} occupy tetrahedral and octahedral coordination sites, respectively.

Ferrites are widely researched materials due to their broad range of technological applications in electronic devices,[2] such as high-speed digital tapes, recording discs, rod antennas, and humidity sensors,[3-6] gas sensor in environmental monitoring,[7,8] permanent magnets,[9] catalytic reactions,[10-12] and as absorbent materials for environmental applications.[13] Their properties are strongly influenced by particle size distributions, particle agglomeration degree and morphologies.[14] Those microstructural parameters can be well controlled during the synthesis. Doping processes of ferrites nanocrystals using different metals, such as zinc,[15,16] nickel,[17] copper,[11] manganese[18] and cobalt[19] are commonly used to improve their electric, catalytic, or magnetic properties.[17,18]

Several methods using chemical synthesis of zinc ferrite nanoparticles have been reported such as coprecipitation,[11,17,18,20] hydrothermal,[14] sol-gel,[19] and polymeric precursors.[21] The properties of these materials are strongly influenced by the chemical composition and microstructure which are significantly dependent on the chemical route used for their synthesis. The most common method used to obtain these doped ferrites is co-precipitation which involves the use of metal salts at different molar ratio (Fe:Metal) in a basic environment (pH > 8).[11,17,18]

In this work, zinc-doped ferrites were prepared and those compounds are spinel systems which present AB_2O_4-type structures, where 8 Zn^{II} and 16 Fe^{III} ions occupy tetrahedral and octahedral sites, respectively, in

*e-mail: aop@ufmg.br; mfflelis@yahoo.com.br
Editor handled this article: Jaísa Fernandes Soares

a crystallographic face-centered cubic unit cell.[16,22] The electric and magnetic properties of these materials are also highly influenced by their cation occupation in tetrahedral and octahedral sites. Due to the relatively small energy difference among Zn^{II} ions in T and M sites,[9,11] cation redistribution is strongly influenced by the annealing temperature and cooling rate used during the synthesis.[22] $Zn_xFe_{(3-x)}O_4$ is an important member of the spinel ferrite family and an efficient photocatalyst mainly due to its ability to absorb visible light.[23-25] The photochemical stability of $Zn_xFe_{(3-x)}O_4$ remarkably promotes an efficient conversion of H_2O_2 into highly reactive HO• radical, addressing its particular interest on the oxidative photocatalytic degradation of organic substrates.[11,12] Some reported data on the use of $Zn_xFe_{(3-x)}O_4$ nanoparticles also showed their hydrophobic and hydrophilic anticancer behavior through local drug delivering systems,[26-29] another very interesting application of these materials.

In this work the synthesis using coprecipitation method and the characterization of zinc-doped ferrite samples is described as well as photocatalysis tests under UV light. The crystallographic and hyperfine structures, along with the cation distribution of the undoped and Zn-doped samples, were assessed by UV-Vis, X-ray absorption (XAS) and ^{57}Fe Mössbauer spectroscopies and X-ray diffraction (XRD). XAS is an ideal technique to investigate the local structure around different cations due to its high chemical selectivity and sensitivity. The influence of the chemical structure on the catalytic efficiency of these zinc ferrite nanocrystals towards the degradation of the indigo carmine dye was also reported in this work which undoubtedly allows a better understanding of the main chemical mechanisms involved in dye degradation process.

Experimental

Synthesis and characterization

Doped ferrites were synthetized by co-precipitation of Zn^{II} and Fe^{III} chlorides in aqueous solutions, at room temperature, through addition of ammonium hydroxide. All chemicals used, $FeCl_3.6H_2O$, $ZnCl_2$, NH_4OH, CH_3COONH_4, HCl and $K_2Cr_2O_7$ were purchased from Vetec (New Química, Vitória-ES, Brazil). The obtained solids were washed with ammonium acetate, dried, and decomposed under N_2 atmosphere at 420 °C for 2 h.[30] A sample of pure magnetite was prepared and used as reference. Total iron was then quantified by using the standard dichromatometric method;[31] in this analysis it was possible to quantify Fe^{II}. In this method the samples were dissolved in HCl aqueous solution under CO_2 atmosphere and titrated with $K_2Cr_2O_7$. Zn content was determined by inductively coupled plasma optical emission spectrometry (ICP-OES) on a PerkinElmer Optima 7000DV.

XRD data were acquired on a Rigaku Geigerflex diffractometer equipped with a Co tube (Kα radiation, λ = 0.17092 nm) and a graphite monochromator using a scanning rate of 1° 2θ min^{-1} and a dwell time of 5 s *per* step. Room-temperature ^{57}Fe Mössbauer spectra were recorded on a conventional transmission constant acceleration spectrometer using a ^{57}Co/Rh source. αFe foil was used to calibrate the Doppler velocity and isomer shift. All spectra were numerically fitted using the least-squares computer program NORMOS-90.[32] Samples were mixed with sugar in order to obtain an averaged Fe density of about 10 mg cm^{-2}. A 13 mm diameter acrylic disc was used as sample holder.

XAS measurements were performed using the DB04-XAFS1 beamline at the National Synchrotron Light Laboratory (LNLS), Campinas, Brazil. All spectra were collected at the Zn K-edge (9659 eV) for $ZnFe_2O_4$ and ZnO (standard) in transmission mode using a Si(111) channel-cut monochromator, previously calibrated using 7.5 µm Zn foil. X-ray absorption near edge structure (XANES) spectra were recorded from 9600 to 9700 eV at 0.5 eV steps with 5 s counting time. Extended X-ray absorption fine structure (EXAFS) data were collected from 9700 to 10700 eV at 3.0 eV steps and with 5 s counting time. EXAFS spectra were numerically treated using the WinXAS algorithm.[33] XANES data were background-corrected by using a polynomial fit in the pre-edge region and normalized in the 9600-9655 eV energy range for Zn samples. The edge position was determined as the zero of the second derivative of experimental spectra. Atomic absorption data were fitted by a cubic spline function in the k^3 space. EXAFS signals, $k^3 \cdot \chi(k)$, were Fourier-transformed using a Bessel window to obtain the radial distribution function (RDF). As we were interested only in the first coordination shell, which gives information about Zn^{II} sites, we applied a Fourier back-transformation only to the first RDF peak and fitted the obtained $\chi(k)$ functions by the least-squares procedure, using experimental phases and amplitudes extracted from a standard compound, ZnO, which contains 4 Zn–O bonds at 1.98 Å.

Photocatalytic tests

The photocatalytic activity of $Zn_xFe_{(3-x)}O_4$ was assessed by degradation of indigo carmine dye solutions via oxidation processes in the presence of H_2O_2 and UV light or direct photolysis. 20 mg of $Zn_xFe_{(3-x)}O_4$ and 2.0 mL of H_2O_2 aqueous solution (0.028 mol L^{-1}) were mixed and then

added to 50 mL of indigo carmine dye aqueous solution (20 mg L^{-1}, pH 3.0) at room temperature (25 °C). These reaction systems were kept at a distance of 15 cm from a UV lamp (Philips, 80 W). Aliquots were collected at equal time intervals and centrifuged and then their absorbance values were determined as the peak maximum at 610 nm using a Hach DR 5000 UV-Vis spectrophotometer. Dye removal efficiency was then calculated using the concentration values. Photolysis and adsorption tests of indigo carmine in the presence of $Zn_xFe_{(3-x)}O_4$ were also carried out for comparison with the results of oxidation reactions.

Results and Discussion

The chemical formulae obtained through chemical analysis, Table 1, showed that both samples present some degree of oxidation which was confirmed by the presence of cation vacancies. XRD patterns (Figure 1) display reflections that are assigned to the cubic phase of $ZnFe_2O_4$ (franklinite, JCPDS card number 22-1012).[34] Lattice parameters (Table 1) were calculated through the analysis of (220), (311) and (440) reflections using UnitCell software.[35] $ZnFe_2O_4$ spinel cubic phase is reportedly stable at temperatures higher than 360 °C.[35] Mean particle size was estimated from the (311) reflection peak breadth, using the Scherrer's equation.[36,37] The lattice parameter value for this prepared magnetite (Fe_3O_4) (a = 0.83889(5) nm) is well consistent with that of the standard magnetite (a = 0.8396 nm, JCPDS card No. 19-0629). This result strongly suggests that if ferrous iron oxidation occurred, it did not lead to detectable changes in the crystalline structure of the obtained magnetite. For the zinc doped spinel, $Zn_xFe_{(3-x)}O_4$, the cubic lattice dimension (a = 0.84157(5) nm) was found to be higher than that of Fe_3O_4.[35,38] This cell expansion of $Zn_xFe_{(3-x)}O_4$ was expected as the ionic radii of Zn^{II} in tetrahedral and octahedral sites are 60 and 75 pm, respectively, which in both cases are higher than the ionic radii of Fe^{III} (high spin), which is 49 or 65 pm, in tetrahedral and octahedral sites, respectively.[37] Mean crystallite sizes calculated for Fe_3O_4 and $Zn_xFe_{(3-x)}O_4$ were 46 and 22 nm, respectively.

The full width at half maximum (FWHM) values calculated through least squares-fitting of (220), (311) and (440) reflections of $Zn_xFe_{(3-x)}O_4$, are approximately greater than twice the values obtained for the Fe_3O_4 sample (Table 2).

Table 1. Chemical formula, unit cell parameter (a), and mean crystallite size (D) of samples

Sample	Chemical formula	a / nm	D / nm
Fe_3O_4	$Fe^{III}_{2.135}Fe^{II}_{0.798}\otimes_{0.067}O_4^{-II}$	0.83889(5)	46
$Zn_xFe_{(3-x)}O_4$	$Fe^{III}_{2.000}Fe^{II}_{0.544}Zn^{II}_{0.457}\otimes_{-0.001}O_4^{-II}$	0.84157(5)	22

⊗ = cation vacancy. Numbers in parentheses are uncertainties over the last significant digit of the numerical value, as estimated from the standard deviation obtained from UnitCell code.[37]

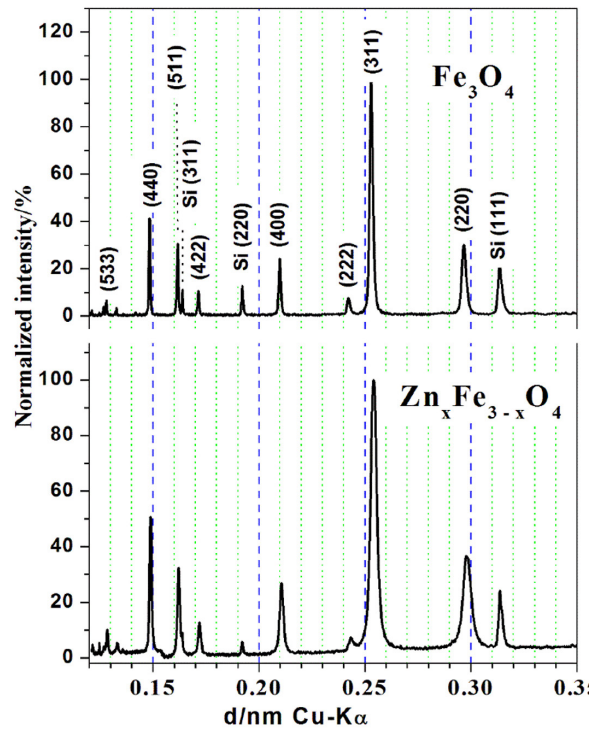

Figure 1. XRD patterns for the Fe_3O_4 and $Zn_xFe_{(3-x)}O_4$ samples.

Table 2. Full width at half maximum (FWHM) of $K_{\alpha 1}$ Lorentzian components obtained from least squares-fitting the (220), (311) and (440) reflection peaks for the $Zn_xFe_{(3-x)}O_4$ and Fe_3O_4 samples

Sample	FWHM / nm		
Diffraction peak	(220)	(311)	(440)
Fe_3O_4	0.00183(2)	0.00128(2)	0.00054(2)
$Zn_xFe_{(3-x)}O_4$	0.00293(3)	0.00257(2)	0.00092(1)

The room-temperature ^{57}Fe Mössbauer spectrum (Figure 2) of the Fe_3O_4 sample showed two well-defined sextets assignable to iron in both tetrahedral and octahedral sites of the spinel structure. Experimental data were fitted by two Lorentzian-shaped sextets for each sub-spectrum, assignable to each Fe–O coordination sites, Table 3. These Mössbauer parameters indicate the coexistence of two populations of magnetite in the sample.[20]

In a stoichiometric magnetite, the atomic ratio, $R_{atomic} = \frac{\left\{Fe^{\frac{III}{II}}\right\}}{\left[Fe^{III}\right]}$, is equal to 2. To draw the corresponding relative subspectral Mössbauer area (RA) ratio, the

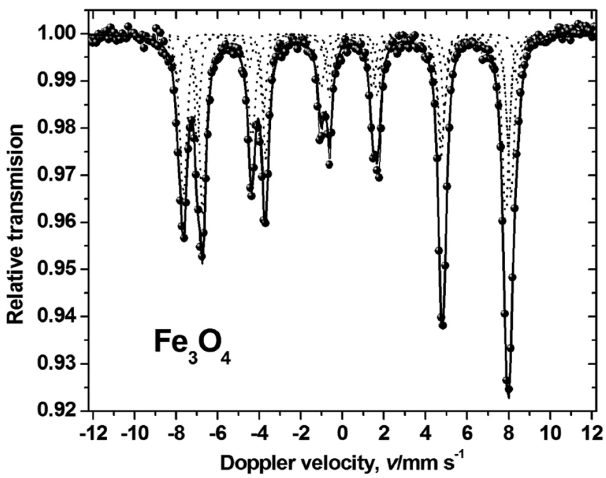

Figure 2. ^{57}Fe Mössbauer spectrum of Fe_3O_4 sample at room temperature. Solid lines represent the fit of theoretical Lorentzian functions to the experimental data.

Table 3. ^{57}Fe Mössbauer parameters of Fe_3O_4 sample

Site	B_{hf} / T	δ / (mm s^{-1})	$2\varepsilon_Q$ / (mm s^{-1})	RA / %
Tetrahedral RA = 47%	48.9(1)	0.32(1)	0.02(1)	40
	50.6(1)	0.36(1)	0.01(2)	7
Octahedral RA = 53%	45.2(1)	0.65(1)	0.03(1)	40
	46.4(1)	0.63(1)	0.06(1)	13

B_{hf}: hyperfine field; δ: isomer shift relative to the αFe foil; $2\varepsilon_Q$: quadrupole shift; RA: relative subspectral area. Numbers in parentheses are uncertainties over the last significant digit of the numerical value, as output by the least squares fitting computer program.

recoilless fraction (f) must be fully taken into consideration. It is reported that the fraction values of M sites is 6% below those of T sites,[39,40] for a pure and stoichiometric magnetite. In view of this, the ratio $R_{RA} = \frac{RA_{\{Fe^{III}_{II}\}}}{0.94} / RA_{[Fe^{III}]} = 2$, or $R_{RA} = \frac{RA_{\{Fe^{III}_{II}\}}}{RA_{[Fe^{III}]}} = 1.88$. The experimental relative subspectral ratio area, RA, was 1.3 for the Fe_3O_4 sample. This result implies that the sample experienced some $Fe^{II} \rightarrow Fe^{III}$ oxidation, as confirmed by its corresponding chemical composition (Table 1), in the octahedral sites.

The Mössbauer spectrum (Figure 3) of $Zn_xFe_{(3-x)}O_4$ is much more complex compared to the one of stoichiometric frankilinite. The end-member franklinite $ZnFe_2O_4$ itself has a normal spinel structure, with all Zn^{II} located in T sites: its Mössbauer spectrum is composed by only one ferric doublet, with isomer shift relative to the αFe and quadrupole splitting values of δ = 0.348 mm s^{-1} and $2\varepsilon_Q$ = 0.348 mm s^{-1}, respectively.[23] Franklinite is an anti-ferromagnetic oxide,[41] in which Zn occupies one tetrahedral site and Fe^{III} the octahedral B-sites.[42] The antiferromagnetism of this compound at room temperature is due to the predominantly negative super-exchange interaction among Fe^{III} ions at M sites.[23] On the other hand, if a solid solution composed of an intermediate phase between magnetite and franklinite is formed, at least two sextets corresponding to iron in T and M sites appear, despite the putative preference of Zn^{II} for T sites. Regarding the Mössbauer results (Figure 3) of this $Zn_xFe_{(3-x)}O_4$ sample, two broad and asymmetric sextets were observed, indicating partial replacement of Fe^{III} by Zn^{II}, mainly at tetrahedral sites of the spinel structure. The probability profiles of hyperfine field values for both coordination sites are, through this fitting model, linearly correlated with values of isomer shifts displayed in Figure 3.

For $Zn_xFe_{(3-x)}O_4$ the probability profiles of the hyperfine fields, Figure 3, showed a maximum at 43.1 and 47.6 T for tetrahedral sites and 39.4; 42.9 and 45.7 T for octahedral sites.

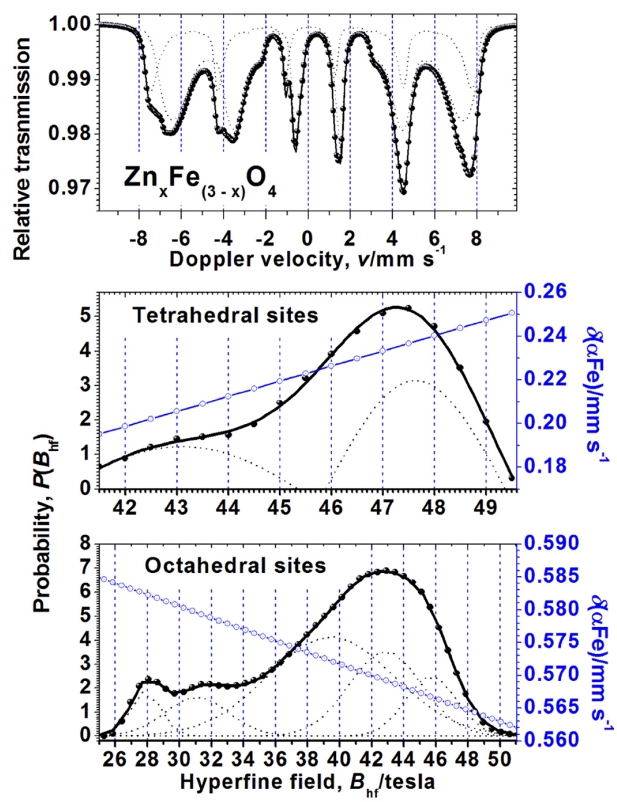

Figure 3. Independent hyperfine field distributions models of ^{57}Fe Mössbauer spectrum of the Zn-doped magnetite sample ($Zn_xFe_{(3-x)}O_4$). The probability profiles of the hyperfine fields for tetrahedral (maximum probabilities at 43.1 and 47.6 T) and octahedral sites (main peaks of maximum probabilities at 39.4; 42.9 and 45.7 T) of the spinel structure are displayed together with the corresponding isomer shift values relative to the αFe foil, linearly varying with values of the field.

EXAFS experiments were carried out in Zn-doped magnetite sample in order to determine the Zn local

structure. For the raw EXAFS spectrum of the Zn sample (Figure 4a) a good signal-to-noise ratio was achieved. $\chi(k)$ functions weighted by k^3 were obtained from the Fourier transform of these spectra (Figure 4b) and adjusted using experimental phase shift and amplitude values extracted from ZnO spectra (standard material). The $k^3 \cdot \chi(k)$ functions were Fourier transformed over the 2.3-9.2 Å range using the Kaiser-Bessel window to obtain the partial RDF functions (Figure 5a) in which the peaks represent shells of atoms surrounding Zn atoms. As depicted in Figure 5a, the RDF of ZnO and $Zn_xFe_{(3-x)}O_4$ are relatively similar with the first peak located at 1.51 Å. This first peak is associated to Zn–O interactions (first coordination shell). The second peak is associated to Zn–Zn and Zn–Fe interactions. EXAFS parameters of $Zn_xFe_{(3-x)}O_4$ (Table 4) were obtained from the fitting of the Fourier back-transformed RDF functions of the first coordination shell using experimental phases and amplitudes extracted from the experimental data obtained from standard ZnO, Figure 5b. These parameters are in excellent agreement with those found for $Zn_xFe_{(3-x)}O_4$.[34] The coordination number obtained for Zn–O shell, 3.58, showed that Zn ions mainly occupy the T site, in agreement with experimental results of co-precipitation followed by annealing at 420 °C.[16,22]

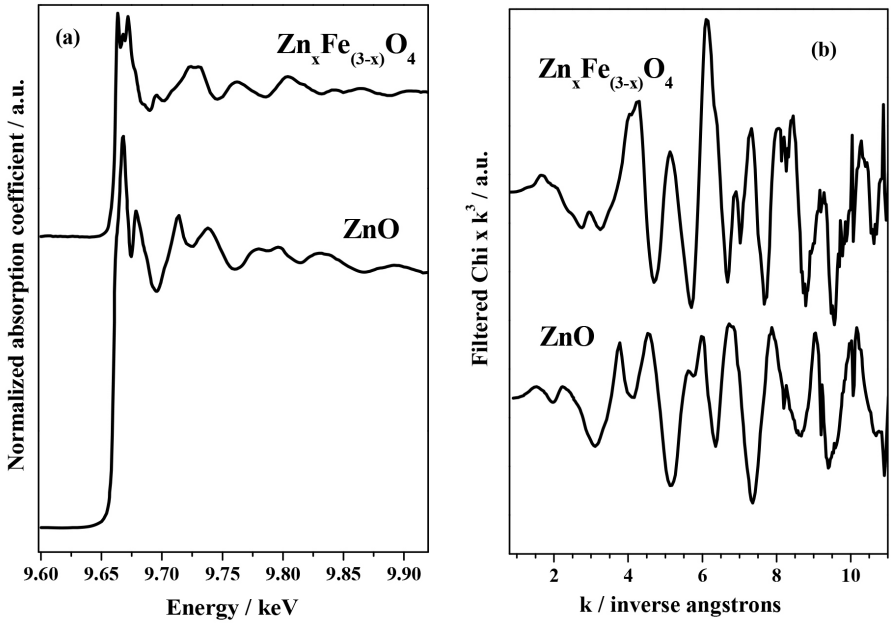

Figure 4. (a) Raw EXAFS spectra and (b) k^3-weighted $\chi(k)$ spectra of ZnO and $Zn_xFe_{(3-x)}O_4$.

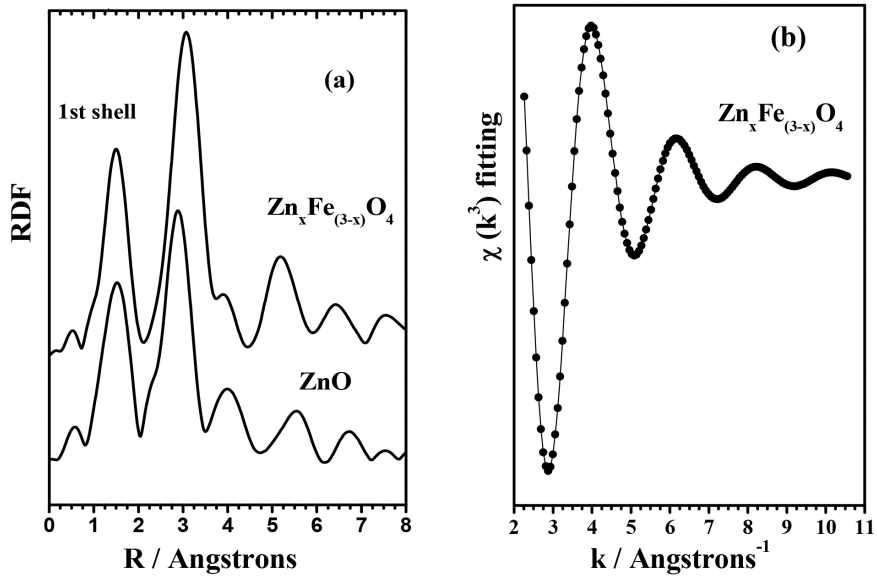

Figure 5. (a) Radial distribution function (RDF) and (b) experimental (dots) and calculated (solid line) Fourier back-transformed RDF functions obtained for the first shell of $Zn_xFe_{(3-x)}O_4$.

Table 4. Zn–O coordination distance (R), number of oxygen atoms (N), and Debye-Waller factor (σ^2) of nonlinear fitting of filtered EXAFS spectra for the first zinc-oxygen coordination shell

Sample	N	R / Å	σ^2 / Å^2	ΔE_0
$Zn_xFe_{(3-x)}O_4$	3.58	1.96	−0.0069(1)	−2.94

The uncertainties on N and R values are 0.5% and 0.02 Å, respectively. ΔE_0: energy shift.

Figure 6 shows the XANES spectra obtained for $Zn_xFe_{(3-x)}O_4$ sample and ZnO. XANES spectra of compounds containing Zn in tetrahedral sites present more features than those of Zn in tetrahedral sites.[33] The energy of the first edge feature in the XANES spectrum is indicative of Zn^{II} coordination; generally, tetrahedral edges are shifted to lower energies by 2 eV or more compared to octahedral Zn edges.[33] In $Zn_xFe_{(3-x)}O_4$ and ZnO spectra, edge positions were located at 9661 and 9659 eV, respectively, indicative of Zn^{II} occupying tetrahedral sites. The XANES spectrum of $Zn_xFe_{(3-x)}O_4$ sample was very similar to that reported in previous studies[34,35] for franklinite (stoichiometric $ZnFe_2O_4$), which shows two peaks after the first peak, at 9668.0 and 9671.8 eV. In the spectrum of $Zn_xFe_{(3-x)}O_4$ sample these two peaks were located at 9663.0 and 9672.0 eV. Basically, Zn doping causes rearrangement of Fe^{III} to tetrahedral sites.

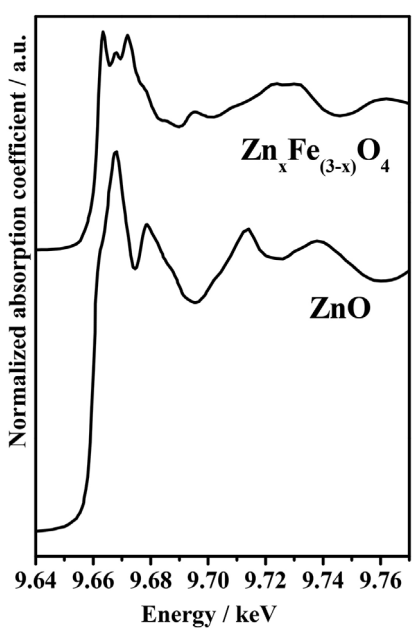

Figure 6. Normalized XANES spectra of $Zn_xFe_{(3-x)}O_4$ and ZnO.

The photocatalytic activity of $Zn_xFe_{(3-x)}O_4$ towards indigo carmine degradation under UV irradiation was evidenced by a reduction in UV-Vis absorption at 610 nm (Figure 7a). Five experiments were carried out using an organic dye and (*i*) catalyst, (*ii*) UV light (photolysis), (*iii*) catalyst + UV light, (*iv*) catalyst + H_2O_2 solution (Fenton reaction), and (*v*) H_2O_2 solution + UV light (photo-Fenton reaction). The exposition of indigo carmine only to UV light (*ii*) or $ZnFe_2O_4$ (*i*) did not result in dye degradation. Fenton (*iv*) and H_2O_2 + UV light (*v*) experiments resulted in low degradation efficiencies (40%) after 100 min of reaction. Compared with Fenton reaction, photo-Fenton significantly increased the degradation rate, affording a discoloration efficiency of more than 98% after 100 min (Figure 7b). In photo-Fenton reactions, active oxidizing species such as $HO^{\bullet}$ are produced in a very short time interval compared with Fenton reactions, resulting in rapid oxidation of contaminants, similar behavior was previously observed in the literature.[11,12]

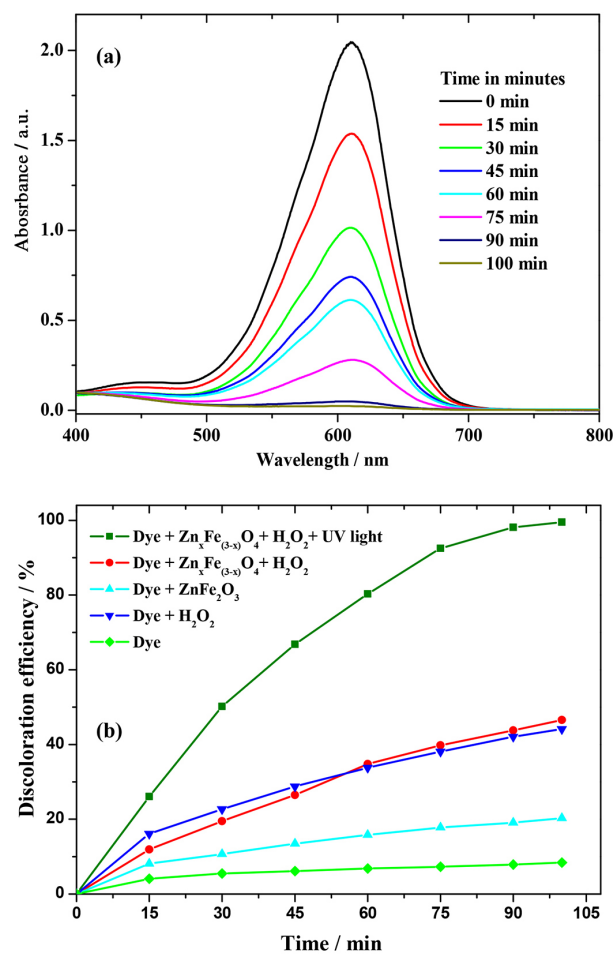

Figure 7. (a) UV-Vis spectral absorption changes of indigo carmine dye aqueous solution (50 mL, 20 mg L^{-1}) photodegraded (experimental conditions: $Zn_xFe_{(3-x)}O_4$ = 20 mg, H_2O_2 = 0.028 mol L^{-1}, T = 25 °C, pH 3.0) (b) Discoloration efficiency of indigo carmine solution as a function of reaction time under different conditions.

The mechanisms of photo-Fenton oxidation reactions are well explained in the literature.[43] UV-Vis spectra of $ZnFe_{2+z}O_4$ samples exhibit intensive absorption in a wide wavelength range from UV to visible light and Šutka *et al.*[16]

showed that the energies of the direct band-gaps when z = 0.0, 0.05, 0.1 and 0.15, vary from 2.02, 1.98, 1.92 and 1.90 eV, respectively.

Figure 8 shows UV-Vis absorption bands of indigo carmine solutions before and after discoloration as a function of time. In these spectra the absorption bands below 340 nm are associated to the absorption of degradation products, and the bands at 280 nm are related to the absorption of the aromatic rings of the indigo carmine structure. According to Terres *et al.*[43] and Giri *et al.*[44] decolorization of indigo carmine is likely to produce intermediates such as 2-amino-5(sodium benzenesulfonate)-benzoic acid, anthranilic acid, benzoic acid, and aniline. These fragments present absorption bands below 340 nm due to the presence of an aromatic benzene ring. The spectra showed in Figure 8, display the absorption bands at 246 nm, suggesting the formation of those afore mentioned reaction intermediates. Throughout the reaction, the intensity of these absorption bands, in the range of 300-400 nm, decreases until completely disappears after 300 min indicating the degradation of the intermediate species. Absorption bands below 230 nm are associated to the residual hydrogen peroxide which absorbs in this spectral range.[43,44]

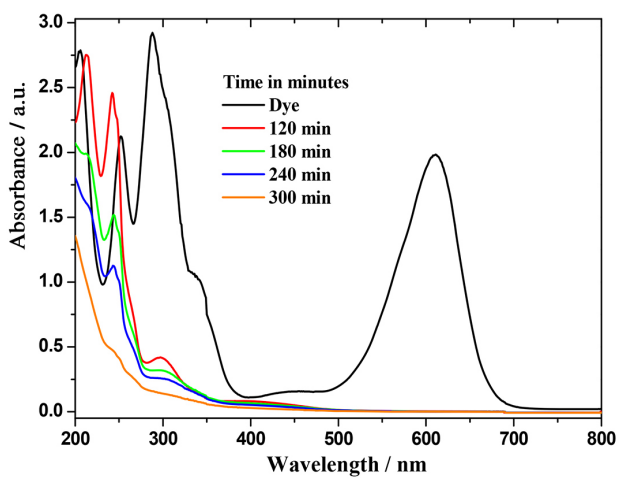

Figure 8. UV-Vis spectral absorption changes of indigo carmine solution before and after discoloration as a function of reaction time (200-800 nm range shown).

Conclusions

The effect of Zn-doping in Fe_3O_4 nanoparticles through the chemical coprecipitation route was investigated. Structural information of this Zn-ferrite was assessed by XAS, XRD and ^{57}Fe Mössbauer spectroscopy. XRD measurements indeed confirmed the formation of a cubic spinel phase, of the *Fd3m* space group; and it was observed that the cell dimension increase and the average crystal size decrease with Zn-doping. ^{57}Fe Mössbauer data revealed that Zn^{II} cations replace Fe^{III} ions in tetrahedral sites. EXAFS results confirm that dopant Zn ions mainly occupy tetrahedral sites. Photo-Fenton tests showed that the use of this spinel ferrite powders showed a significant catalytic efficiency, on degrading 98% of aqueous indigo carmine after 100 min reaction. This zinc-doped $Zn_xFe_{(3-x)}O_4$ ferrite was revealed to be highly efficient as catalyst, and it opens many more perspectives on the development of new related Zn ferrites prepared through different chemical routes with high photocatalytic performance in order to promote environmental remediation of wastewater of natural water bodies.

Acknowledgments

The authors thank the Brazilian Synchrotron Light Laboratory (LNLS, grant No. D04B-XAFS1 No. 4845/05) and the Espírito Santo Research Foundation (FAPES) for the financial support. JDF is indebted to Brazilian National Council for the Scientific and Technological Development (CNPq) for the research grant No. 304958/2017-4.

Author Contributions

The authors Luciana B. Biazati and Lucas Lorenzini were responsible for the investigation, data curation, formal analysis (synthesis, sample preparation and analysis); Sandra A. D. Ferreira for investigation, data curation, writing original draft and writing-review and editing; Arilza O. Porto worked in the EXAFS measurements, data analysis data curation and writing and reviewing the manuscript; Eustáquio V. R. de Castro and Marcos B. J. G. de Freitas for conceptualization and writing-review and editing; José D. Fabris worked in the Mossbauer measurements, for conceptualization and writing-review and editing; Maria de Fátima F. Lelis worked in the XRD and Mossbauer measurements, conceptualization, project administration and writing-review and editing.

References

1. Music, S. In *Mössbauer Spectroscopy of Sophisticated Oxides*; Vértes, A.; Homonnay, Z., eds.; Akadémiai Kiadó: Budapeste, 1997.
2. Pottker, W. E.; Ono, R.; Cobos, M. A.; Hernando, A.; Araujo, J. F. D. F.; Bruno, A. C. O.; Lourenço, S. A.; Longo, E.; Porta, F. A. L.; *Ceram. Int.* **2018**, *44*, 17290.
3. Dalawai, S. P.; Shinde, T. J.; Gadkari, A. B.; Vasambekar, P. N.; *J. Solid State Electrochem.* **2016**, *20*, 2363.
4. Bindu, K.; Sridharan, K.; Ajith, K. M.; Lim, H. N.; Nagaraja, H. S.; *Electrochim. Acta* **2016**, *217*, 139.
5. Karmakar, M.; Das, P.; Pal, M.; Mondal, B.; Majumder, S. B.; Mukherjee, K.; *J. Mater. Sci.* **2014**, *49*, 5766.

6. Bangale, S.; Bamane, S.; *Carbon: Sci. Technol.* **2013**, *5*, 231.
7. Mukherjee, C.; Mondal, R.; Dey, S.; Kumar, S.; Das, J.; *IEEE Sens. J.* **2017**, *17*, 2662.
8. Liu, Y. L.; Liu, Z. M.; Yang, Y.; Yang, H. F.; Shen, G. L.; Yu, R. Q.; *Sens. Actuators, B* **2005**, *107*, 600.
9. Hankare, P. P.; Jadhav, S. D.; Sankpal, U. B.; Patil, R. P.; Sasikala, R.; Mulla, I. S.; *J. Alloys Compd.* **2009**, *488*, 270.
10. Rashad, M. M.; Mohamed, R. M.; Ibrahim, M. A.; Ismail, L. F. M.; Abdel-Aal, E. A.; *Adv. Powder Technol.* **2012**, *23*, 315.
11. Rocha, A. K. S.; Magnago, L. B.; Santos, J. J.; Leal, V. M.; Marins, A. A. L.; Pegoretti, V. C. B.; Ferreira, S. A. D.; Lelis, M. F. F.; Freitas, M. B. J. G.; *Mater. Res. Bull.* **2019**, *113*, 231.
12. Ferreira, S. A. D.; Donadia, J. F.; Gonçalves, G. R.; Teixeira, A. L.; Freitas, M. B. J. G.; Fernandes, A. R.; Lelis, M. F. F.; *J. Environ. Chem. Eng*. **2019**, *7*, 103144.
13. Rashdan, S. A.; Hazeem, L. J.; *Arab J. Basic Appl. Sci.* **2020**, *27*, 134.
14. Li, M.; Liu, X.; Xu, T.; Nie, Y.; Li, H.; Zhang, C.; *J. Magn. Magn. Mater*. **2017**, *439*, 228.
15. Li, F.; Wang, H.; Wang, L.; Wang, J.; *J. Magn. Magn. Mater*. **2007**, *309*, 295.
16. Šutka, A.; Pärna, R.; Kleperis, J.; Käämbre, T.; Ilona, P.; Korsaks, V.; Malnieks, K.; Grinberga, L.; Kisand, V.; *Phys. Scr.* **2014**, *89*, 044011.
17. Magnago, L. B.; Rocha, A. K. S.; Pegoretti, V. C. B.; Ferreira, S. A. D.; Lelis, M. F. F.; Freitas, M. B. J. G.; *Ionics* **2018**, *25*, 2361.
18. Morais, V. S.; Barrada, R. V.; Moura, M. N.; Almeida, J. R.; Moreira, T. F. M.; Gonçalves, G. R.; Ferreira, S. A. D.; Lelis, M. F. F.; Freitas, M. B. J. G.; *J. Environ. Chem. Eng*. **2020**, *8*, 103716.
19. Amiri, M.; Salavati-Niasari, M.; Akbari, A.; Gholami, T.; *Int J. Hydrogen Energy* **2017**, *42*, 24846.
20. Lima, E. S.; Costa, L. S.; Sampaio, G. R. L. M.; Oliveira, E. S.; Silva, E. B.; Nascimento, H. O.; Nascimento, R. F.; Moura, K. O.; Basto-Neto, M.; Loiola, A. R.; Sasaki, J. M.; *J. Braz. Chem. Soc.* **2019**, *30*, 882.
21. Martins, M. L.; Florentino, A. O.; Cavalheiro, A. A.; Silva, R. I. V.; Santos, D. I.; Saeki, M. J.; *Ceram. Int.* **2014**, *40*, 16023.
22. Shahraki, R. R.; Ebrahim, S. A. S.; Masoudpanah, S. M.; *J. Supercond. Novel Magn.* **2015**, *28*, 2143.
23. Kefeni, K. K.; Msagati, T. A. M.; Mamba, B. B.; *Mater. Sci. Eng., B* **2017**, *215*, 37.
24. Sun, Y.; Wang, W.; Zhang, L.; Sun, S.; Gao, E.; *Mater. Lett.* **2013**, *98*, 124.
25. Nan, C.; Fan, G.; Fan, J.; Li, F.; *Mater. Lett.* **2013**, *106*, 5.
26. Wu, J.; Pu, W.; Yang, C.; Zhang, M.; Zhang, J.; *J. Environ. Sci.* **2013**, *25*, 801.
27. Mahnaz, A.; Salavati-Niasari, M.; Akbari, A.; *Adv. Colloid Interface Sci.* **2019**, *265*, 29.
28. Priyanka, S.; Rupali, R.; Kalyan, M.; *J. Magn. Magn. Mater.* **2019**, *475*, 130.
29. Oh, Y.; Moorthy, M. S.; Manivasagan, P.; Bharathiraja, S.; Oh, J.; *Biochimie* **2017**, *133*, 7.
30. Abreu Filho, P. P.; Pinheiro, E. A.; Galembeck, F.; Labaki, L. C.; *React. Solids* **1987**, *3*, 241.
31. Jeffery, P. G.; Hutchison, D.; *Chemical Methods of Rock Analysis*, 3rd ed.; Pergamon Press: Oxford and New York, 1981.
32. Brand, R. A.; *Normos-90 Laboratoriumfür Angewandte Physik*; Universität Duisburg: Duisburg, Germany, 1999.
33. Ressler, T. J.; *J. Synchrotron Radiat*. **1998**, *5*, 118.
34. *Mineral Powder Diffraction File-Data Book*; JCPDS, International Center Diffraction Data: USA, 1980.
35. Holland, T. J. B.; Redfern, S. A. T.; *Mineral. Mag.* **1997**, *65*, 61.
36. Cullity, B. D.; *Elements of X-ray Diffraction*, 2nd ed.; Addison-Wesley: London, 1978.
37. Kaye, G. W. C.; Laby, T. H.; *Table of Physical and Chemical Constants (and Physical and Chemical Functions)*; Longman: London and New York, 1973.
38. Maiti, D.; Saha, A.; Devi, P. S.; *Phys. Chem. Chem. Phys.* **2016**, *18*, 1439.
39. Sawatzky, G. A.; Van der Woude, F.; Morrish, A. H.; *Phys. Rev. J. Arch.* **1969**, *187*, 747.
40. Sawatzky, G. A.; Van der Woude, F.; Morrish, A. H.; *Phys. Rev. J. Arch.* **1969**, *183*, 383.
41. Costa, A. C. S.; Souza Jr., I. G.; Batista, M. A.; Silva, K. L.; Bellini, J. V.; Paesano Jr., A.; *Hyperfine Interact*. **2007**, *175*, 103.
42. Costa, A. C. S.; Souza Jr., I. G.; Batista, M. A.; Lopes, D. A.; Silva, K. L.; Bellini, J. V.; Paesano Jr., A.; *Hyperfine Interact*. **2007**, *176*, 107.
43. Terres, J.; Battisti, R.; Andreaus, J.; Jesus, P. C.; *Biocatal. Biotransform.* **2014**, *32*, 64.
44. Giri, R. R.; Ozaki, H.; Takayanagi, Y.; Taniguchi, S.; Takanami, R.; *Int. J. Environ. Sci. Technol*. **2011**, *8*, 19.

Submitted: May 19, 2021
Published online: September 16, 2021